In-Depth Investigation of Manganese Dioxide as Pseudocapacitive Electrode in Lithium- and Sodium-Doped Ionic Liquids

Thibaud Guillemin, Camille Douard, Anthony Impellizzeri, Christopher Ewels, Bernard Humbert, Christophe Lethien, Scott Wilfred Donne, Jean Le Bideau, Thierry Brousse

In-depth investigation of manganese dioxide as pseudocapacitive electrode in lithium- and sodium-doped ionic liquids

Thibaud Guillemin[1,2], Camille Douard[1,2], Anthony Impellizzeri[1], Christopher P. Ewels[1], Bernard Humbert[1], Christophe Lethien[2,3,4], Scott W. Donne[5,Z], Jean Le Bideau[1,2,Z] and Thierry Brousse[1,2,Z]

Affiliation(s):
[1] Nantes Université, CNRS, Institut des Matériaux de Nantes Jean Rouxel, IMN, F-44000 Nantes, France
[2] Réseau sur le Stockage Electrochimique de l'Energie (RS2E), CNRS FR 3459, 33 rue Saint Leu, 80039 Amiens Cedex, France
[3] Institut d'Electronique, de Microélectronique et de Nanotechnologies, Université de Lille, CNRS, Université Polytechnique Hauts-de-France, UMR 8520 - IEMN, F-59000 Lille, France
[4] Institut Universitaire de France (IUF), Paris – France
[5] University of Newcastle, Discipline of Chemistry, Callaghan NSW 2308, Australia

[z] Corresponding Authors E-mail Addresses : thierry.brousse@cnrs-imn.fr , jean.lebideau@cnrs-imn.fr , scott.donne@newcastle.edu.au

Abstract

We investigate the contribution of pseudocapacitance to the overall capacitance of MnO_2 electrodes in pure and alkaline-doped ionic liquids via two spectroscopic methods: step potential electrochemical spectroscopy (SPECS) and *in situ* Raman spectroscopy. For both characterization methods, thin-film electrodes of birnessite-like amorphous MnO_2 were cycled in Ethyl-3-methylimidazolium bis(trifluoromethanesulfonyl)imide, pure or doped with lithium or sodium. SPECS allows determination of the influence of the electrolyte composition on the electrochemical behavior of the MnO_2 electrodes. Pseudocapacitive charge storage can account for over half of the total capacitance with alkaline-doped ionic liquids. *In situ* Raman spectroscopy provided insight into the reversible ion intercalation in the MnO_2 structure, which appears to be controlled by $EMIm^+$ cations. These findings are supported by density functional theory (DFT) calculations, which further help unveil the charge storage mechanism in birnessite-like amorphous MnO_2 thin films operated in pure and alkaline-doped ionic liquids.

Introduction

As the demand for energy increases, electrochemical energy storage systems (EESS) are becoming more important for various applications, ranging from small devices for the Internet of Things, to large scale grid storage. The need for improved performance and safety, as well as minimizing environmental impact, has prompted the search for new materials. Accordingly, ionic liquids (ILs) are a promising alternative to organic electrolytes for EESS, including supercapacitors. These electrolytes have distinctive qualities, especially thanks to their solvent-free composition [1–3].

Regarding supercapacitors, these devices require a higher energy density to become competitive. An interesting way to improve their energy density is through the use of pseudocapacitive materials, which exhibit faradaic reactions with fast kinetics, as well as electrochemical signatures similar to those of capacitive reactions [4]. One such material is MnO_2, which is currently mostly tested with water-based electrolytes [5–8]. The use of pseudocapacitive MnO_2 has been shown to perform well in ILs [9,10], but the mechanisms induced in this environment, with the absence of solvent, must differ from that in aqueous electrolytes. The use of spectroscopy methods on MnO_2 electrodes cycled in ILs helps to investigate pseudocapacitive behavior in these environments.

Among other electrochemical characterization methods, step potential electrochemical spectroscopy (SPECS) is a recently developed technique providing performance information, as well as to separate the total current into several contributions [11–13]. This method consists of applying a series of small potential steps, separated by resting times, to allow the system to reach quasi-equilibrium. Contributions from fast process, such as electrochemical double layer capacitance (EDLC) and pseudocapacitance, and slow processes, such as diffusion in the materials structure and side reactions, can be separated thanks to this technique. For each of these separated contributions, SPECS can provide insight into various charge storage processes and performance data from cyclic voltammetry at different scan rates.

To have a more complete view, *in situ* Raman spectroscopy was also performed on a system of similar configuration. MnO_2 Raman signature is mostly visible between 400 and 800 cm^{-1} and displays two main bands, called ν_1 and ν_2 [14]. For the birnessite structure of MnO_2, ν_1 and ν_2 bands are located between 620 – 650 cm^{-1} and 580 – 590 cm^{-1}, respectively [15], and they are highly impacted by the crystallinity of the material (low crystallinity is linked to poor definition) [16]. The birnessite structure is formed from parallel layers of [MnO_6] octahedra sharing edges. The ν_1 and ν_2 Raman bands correspond to specific Mn – O bond vibrations, linked to symmetric stretching and bending in the basal plan of the octahedra, respectively [16–19]. The position of these two bands in the Raman spectrum is dependent on the strength of the Mn – O bonds in the octahedra, and by extension, the interlayer spacing. Literature *in situ* Raman spectroscopy on birnessite MnO_2 electrodes cycled in aqueous electrolyte found a reversible evolution of the bands position, which was linked to the insertion and disinsertion of cations in the interlayer during cycling [14,16,20,21].

A wavenumber increase of the ν_1 band has been observed with the deintercalation of alkali metal cations from MnO_2 (oxidation), which was attributed to a change in the oxidation state of manganese and weakening of the interactions between layers, hence increasing their spacing.

Conversely, intercalation of the alkali metal cations (reduction of manganese) resulted in a decrease in the wavenumber of ν_1. This is also related to a partial reduction of Mn^{IV+} to Mn^{III+} corresponding to a shortening of the Mn – O bonds, stiffening of the layers and lowering the interlayer distance. The ν_2 wavelength shifted during electrode cycling but in the opposite way to ν_1, which leads to more separated bands and better spectral resolution when MnO_2 is oxidized.

Ultimately, replacing the aqueous electrolyte with an ionic liquid is completely modifying the MnO_2 environment and so a different mechanism may occur, even with alkali metal cation-doped ionic liquids [22].

Experimental

Electrodes preparation.

The 16 mm² footprint area electrodes used for SPECS measurements were obtained following procedures reported in earlier studies [10,23–25]. These electrodes were composed of microtubes (110 µm high, 4 and 2 µm of external and internal diameter, respectively) obtained with microelectronic processes, which allowed for an area enlargement factor (AEF) of 40. The 3D microstructure of the electrodes was obtained by etching a silicon wafer according to a pattern controlled by photolithography. The etching was performed by deep reactive-ion etching (DRIE) up to the desired depth of 110 µm between the microtubes and 55 µm in the microtubes. Once the silicon etching was complete, and the photoresist mask cleaned, the silicon wafer was conformally coated by Atomic Layer Diffusion (ALD) with, firstly, 100 nm of alumina (Al_2O_3) as an insulator, and then 40 nm of platinum (Pt) as the current collector. Electrodes used for Raman characterization were commercial 3-electrodes systems from Dropsens (C550) with a 16 mm^2 platinum working electrode, a platinum counter electrode and a silver quasi-reference, all on the same surface.

In order to deposit the MnO_2, electrodes were firstly submitted to a cleaning process. They were immersed in an aqueous 0.1 M H_2SO_4 solution with a platinum wire counter electrode and a Ag/AgCl reference electrode. Cyclic voltammetry was applied to the working electrode over the potential window -0.35 to 1.50 V vs Ag/AgCl at a 50 $mV.s^{-1}$ until the disappearance of irreversible redox peaks. The conformal MnO_2 thin film was then obtained by pulsed electrodeposition. The electrode was placed in an aqueous solution of 0.1 M $MnSO_4$ + 0.1 M H_2SO_4, facing a platinum wire counter electrode and Ag/AgCl reference electrode. Two “pulse” steps of 0.3 s duration each (one potentiostatic step at 1.15 V vs Ag/AgCl and one is at open circuit potential) were alternated to deposit a thin film of MnO_2.

Electrolyte preparation.

For electrochemical and spectroscopic characterization, three electrolytes were prepared with ethyl-3-methylimidazolium bis(trifluoromethanesulfonyl)imide (EMImTFSI) ionic liquid (99.9% purity and < 50 ppm H_2O, from Solvionic); i.e., pure EMImTFSI, EMImTFSI with 0.5M lithium bis(trifluoromethanesulfonyl)imide (LiTFSI), and EMImTFSI with 0.5M

sodium bis(trifluoromethanesulfonyl)imide. The ILs were stored under a passive argon atmosphere (< 0.1 ppm H_2O and < 0.1 ppm O_2).

Among others, these ILs ionic conductivities and behaviors as electrolyte for pseudocapacitors were investigated in previous work [25]. Their ionic conductivity is between 1 - 3 $mS.cm^{-1}$ at RT. The concentration of added alkaline salts was also chosen according this previous work where 0.5M of LiTFSI and NaTFSI allow to show clear performance differences from pure IL without reaching mixture saturation.

MnO_2 thin film characterization with SEM.

The thickness of the MnO_2 deposit was estimated by comparing electrode microstructures before and after electrodeposition by scanning electron microscopy (SEM) on a Merlin Zeiss Field Effect microscope. Indeed, the conformality of the deposit was verified by measuring the width of the microtubes on a cross section of the electrode. The thickness of the deposit was then estimated for each electrode by measuring the differences in sizes (microtubes width and hole diameter) on a plan view of a microtube before and after the deposit (see Figure S1). This method ensures a consistent homogeneous MnO_2 deposit on each electrode. By inspecting the surface of the MnO_2 closely, SEM characterization suggested the structure of the deposit. Indeed, previous work by our team on these mostly poorly crystallized MnO_2 thin-films showed a porous network of small MnO_2 platelets of birnessite structure [26]. This structure shows layers of [MnO_6] octahedra, sharing an edge, between which cations and small molecules can intercalate in trigonal sites when this material is used as an electrode.

Electrochemical cells.

Electrochemical tests were performed in a flat cell for SPECS measurements (See Figure S2). A platinum mesh was used as the counter electrode and a silver wire as a quasi-reference electrode. The working electrode was placed between the two sides of the cell and then secured with two screws. An O-ring between the sides minimizes the risk of electrolyte leakage between the electrode and the cell. The working electrode was covered with 1 mL of electrolyte, and the reference and counter electrodes were immersed in the upper part of the cell. The cell was filled in a glove box with the ionic liquid electrolytes and covered with a paraffin film.

The commercial cells used for *in situ* Raman spectroscopy measurements were used directly after MnO_2 film electrodeposition on the working electrode and the deposit of a drop of electrolyte.

Electrochemical protocol for step potential electrochemical spectroscopy (SPECS).

Before the application of the SPECS program, cyclic voltammetry (CV) at 10 $mV.s^{-1}$ for 150 cycles were performed initially on each electrode between 0 and 1 V vs Ag/Ag^+ until a

stable behavior was reached. The SPECS experiment follows directly these CVs by cycling the electrode with ±10 mV steps, each held for 90 s over the 0 – 1 V vs Ag/Ag^+ potential window.

The current was recorded after each potential step as a function of time, and usually shows a similar evolution with an initial spike in current which then quickly decreased before stabilizing. For each step, the evolution of the current can be fitted to the Eq-1 in which four contributions to the total current have been included; i.e., surface induced capacitive current i_{C1}, porosity induced capacitive current i_{C2}, diffusional current i_D and residual current i_R.

$$i_T = i_{C1} + i_{C2} + i_D + i_R = \frac{E_S}{R_1} * exp\left(\frac{-t}{R_1 * C_1}\right) + \frac{E_S}{R_2} * exp\left(\frac{-t}{R_2 * C_2}\right) + \frac{B}{\sqrt{t}} + i_R \qquad \text{Eq-1}$$

With E_S the size of the potential step (V), R_1 and R_2 equivalent series resistances (Ω), C_1 and C_2 capacitances (F), t the step duration (s) and B a diffusional parameter ($A.s^{1/2}$).

Fitting of Eq-1 to each i-t transient for each step, leads to values for resistance and capacitance across the full potential window of the electrode. The role of each contribution to the total capacitance can be estimate over a wide range of scan rates, from 0.1 to 10^4 $mV.s^{-1}$. Ultimately, cyclic voltammograms at a chosen scan rate can be reconstructed to present the evolution of the four contributions over the potential window [13,27].

In situ Raman spectroscopy: parameters and electrochemical protocol.

Before cycling was performed during *in situ* Raman spectroscopy, the electrodes were cycled at 10 $mV.s^{-1}$ for 150 cycles between -0.3 and 0.7 V vs Ag/Ag^+ (1V potential window) to establish stable cycling behavior. The voltammetric cycle realized during the *in situ* experiment was performed between these potential limits, starting at an initial reduced state of the WE. Nine potentiostatic steps are performed during the cycle (See Figure S3). Every 250 mV, a 15 min potentiostatic stage is applied during which a Raman acquisition is performed. A scan rate of 10 $mV.s^{-1}$ is used between each of these steps during the full cycling of the MnO_2 electrode.

Raman laser power is 0.5 mW and wavelength is 633 nm. These parameters are the best compromise between competing requirements for the MnO_2 and ionic liquid. All spectra were measured between 50 and 1400 cm^{-1} with fifteen accumulations of 30 s each. According to the electrochemical protocol, nine spectra are recorded during electrode cycling (one at the initial state with a reduced WE, four during oxidation and four more during reduction).

Results and Discussion

Current separation following SPECS measurement.

Figure 1 shows the evolution of the current over the duration of a single potentiostatic step in a SPECS experiment. All three electrolyte systems tested, with pure EMImTFSI,

EMImTFSI + 0.5M LiTFSI and EMImTFSI + 0.5M NaTFSI, are presented. An expanded view of the initial current in Figure 1(b) displays a peculiar current variation with the pure EMImTFSI electrolyte. Instead of an initial higher current value and a slow decrease to a stable value, the initial current is low, increasing out to 0,5 s after the potential step. This behavior likely originates from the electrolyte composition. Indeed, EMImTFSI is not containing any alkaline cations, as opposed to the two other electrolytes tested in this work, or aqueous electrolytes used in other works [11,13]. Despite its lower viscosity compared to alkaline cation-doped ionic liquids, the number of charge carriers per volume unit is lower in pure EMImTFSI. This may explain the longer response time following the application of a potential difference. Ternary ionic liquids (EMImTFSI with LiTFSI or NaTFSI) have a similar current response during a potential step, which agrees with their similar composition.

R_1 and C_1, respectively the resistance and capacitance of the contribution i_{C1}, are presented in Figure 2 for each system with a different electrolyte. This contribution is modeling fast electrochemical processes occurring at the surface of the electrodes associated with electrochemical double layer formation. On both graphs, the data are plotted versus the total duration of the SPECS analysis. The oxidation and reduction half-cycles applied to the electrode are separated with the vertical dotted line. The capacitance values are linked to the resistance values; the higher the resistance, the lower the capacitance and the less discernible is its evolution. Also, a contribution to the total current is considered irreversible when its behavior differs between oxidation and reductions stages, as is the case for these parameters.

The value of R_1 changes substantially during oxidation for the system with pure EMImTFSI, then is stabilizing around 20 $\Omega.cm^{-2}$ during reduction. This reveals an irreversible process occurring in the electrode material in this system. It was also noted that the resistance reaches a minimum at 5000 s during the oxidation, corresponding to the capacitance peak observed at the same time. For systems with ternary ILs, resistance values are higher, around 40 $\Omega.cm^{-2}$, due to their higher viscosity, although they are stable over the full cycle. The capacitance of all three systems is similar and comprised between 10 and 60 $mF.cm^{-1}$ with a maximum value at the end of the oxidation half-cycle.

Figure 3 shows the evolution of R_2 and C_2 for the three systems. These parameters are linked to the element i_{C2} in the Eq-1, which is associated with charge storage mechanisms slower than those described by i_{C1}. Indeed, i_{C2} is linked to non-surface charge storage mechanisms and is depicting pseudocapacitance and mechanisms related to MnO_2 porosity.

For each system, the evolution of resistance and capacitance is similar to that observed for R_1 and C_1. Ternary ILs show distinguished behavior ; the one with sodium ions shows lower R_2 values and higher C_2 values over the electrode cycling.

In all cases, R_2 values are much higher than R_1 values. This may be attributed to the kinetic difference between the mechanisms that i_{C1} and i_{C2} are representing. Indeed, due to volume constraints and ionic interactions, the access to MnO_2 porosity and pseudocapacitive reactions are slower than electrostatic ion adsorption (EDLC). However, C_1 and C_2 display similar values, meaning that EDLC and pseudocapacitance both allow similar charge storage

quantity.

The graphs in Figure 4 show the evolution of a diffusional parameter B and the residual current due to parasitic reactions. In Eq-1, these two parameters are represented by i_D and i_R, respectively. These two mechanisms are the slowest and the low scan rate used for the SPECS facilitate their measurement.

The similarity observed between the diffusion parameters with the presence of alkaline ions indicates that lithium and sodium ions interact in similar ways with the IL and MnO_2. The evolution of B in the system with pure EMImTFSI was not expected. It may be explained by the unusual current behavior measured (See Figure 1(b)) which cannot be approached easily with the model. Lastly, the diffusion parameter for pure EMImTFSI should have been small because of the sole presence of $EMIm^+$ ions which have a lower mobility and may be harder to intercalate in MnO_2 porosity and between [MnO_6] layers.

Residual currents are similar for both systems, with increasing values near the potential limits. This contribution is smaller with pure ILs. This may be explained by the presence of the alkaline ions which have more affinity with water, which is itself starting to degrade towards the potential limits.

The behavior of EMImTFSI as an electrolyte presents a unique case, with a current maximum in the i-t transient. This cannot be modeled directly using Eq-1 because of the need for an additional contribution, of reverse polarity, to reflect the slow initial response of this electrolyte. Thus another capacitive contribution i_{C0}, with R_0 resistance and C_0 capacitance, was added to the Eq-1. (similarly to i_{C1} or i_{C2} contributions already used). The graphs in Figure 5 each present the contributions of R_0 and C_0 to the current measured. The evolution of R_0 and C_0 over the SPECS analysis shows non-reversible behavior between oxidation and reduction, which translates to an irreversible transformation in the system.

Following the previous results, the total current measured during the full cycle of oxidation and reduction can be decomposed into four contribution, i_{C1}, i_{C2} i_D and i_R for the three systems. The evolution of the total capacitance, and its contributions, over different scan rates was obtained and is presented in the three following figures. Cyclic voltammetry reconstructions at 1 and 100 $mV.s^{-1}$ showing the role of each contribution were also obtained and displayed below.

Capacitance and CV reconstruction - Pure EMImTFSI.

Figure 6(a) presents the capacitances of the different contributions to the total capacitance of the electrode in pure EMImTFSI as a function of scan rate. In this system, an additional contribution (C_0) was added ; it is related to the i_{C0} parameter previously added to Eq-1 in order to allow the model to fit the measured current (See Figure 1(b)). This contribution is stable and relatively low for the entire range of scan rates (0.1 – 10 000 $mV.s^{-1}$), moreover the values are negative and have no significant effect except at fast sweep rates and to allow for a good fit with Eq-1.

The capacitance values C_1 (EDLC) and C_2 (pseudocapacitance) are contributing to the total capacitance in a similar way, respectively at 35 and 29 $mF.cm^{-2}$ and up to 10 $mV.s^{-1}$. At faster scan rates, C_2 decreases and the majority of the total capacitance is obtained from C_1. At scan rates higher than 100 $mV.s^{-1}$, C_1 is also decreasing. For both C_1 and C_2 values, these declines can be explained by kinetic limitations.

The diffusional contribution is negligible in the entire range of scan rates considered, as well as parasitic reactions at scan rates higher than 1 $mV.s^{-1}$. However, at low scan rates, the parasitic reactions contribute significantly to the total capacitance. For instance, the capacitance plateau for this system between 2 and 20 $mV.s^{-1}$ is 57 $mF.cm^{-2}$.

Cyclic voltammograms at 100 and 1 $mV.s^{-1}$ reconstructed from the preceding SPECS data are presented in Figure 6(b) and (c), respectively. The total current measured matches the usual experimental behavior and values measured at the corresponding scan rates. It must be mentioned that the current of the C_1 contribution is higher than the total current at 100 $mV.s^{-1}$ because of the negative contribution of C_0 as visible in Figure 6(a). The comparison of the two cyclic voltammograms shows the influence of the scan rate on C_2 (pseudocapacitance). Indeed, at high scan rate, the current related to pseudocapacitance is highly resistive and far lower than the current due to the EDLC. At lower scan rates, its behavior and values are similar to the capacitive current. At 1 $mV.s^{-1}$, the current due to parasitic reactions is contributing in a non-negligible way to the total current, in particular around the potential limits where water degradation occurs, which can be due to residual water content in the ILs (< 50 ppm).

Capacitance and CV reconstruction - EMImTFSI + 0,5M LiTFSI.

With EMImTFSI + 0.5M LiTFSI as electrolyte, the contributions to the total capacitance show similar behavior to those described in the previous system (See Figure 7(a)) ; the most significant difference is the largest contribution of the pseudocapacitance, at 40 $mF.cm^{-2}$ until its decrease at scan rates higher than 10 $mV.s^{-1}$. This difference with the system with pure EMImTFSI must be explained by the presence of lithium cations, which have a higher ionic mobility and participate in the pseudocapacitive reactions of MnO_2 [25]. The contribution of the EDLC is lower here (25 $mF.cm^{-2}$). As the system configuration is identical, this may be explained by lower electrode wetting by the electrolyte. This is supported by the increase in viscosity of the IL with the alkaline salt addition. At very low scan rates, the contribution of the diffusion can be observed but remains negligible compared to the other contributions, in particular that of the parasitic reactions. The capacitance plateau in this system is at 67 $mF.cm^{-2}$, between 2 and 20 $mV.s^{-1}$.

The cyclic voltammograms (See Figure 7(b) and (c)) also show more resistive current behavior at higher scan rates, mostly because of the contributions made by pseudocapacitance. As the contribution of C_2 is more significant in this system, the cyclic voltammogram at 1 $mV.s^{-1}$ shows a box-like signature.

Capacitance and CV reconstruction - EMImTFSI + 0,5M NaTFSI.

The capacitance and reconstructed cyclic voltammograms obtained from the system with EMImTFSI + 0.5M NaTFSI are displayed in Figure 8. The same observations can be made here in comparison with the system with lithium ions. The main difference is globally higher values of capacitance, until their decrease due to kinetic limitations. EDLC gives a capacitance of 41 $mF.cm^{-2}$ and pseudocapacitance of 70 $mF.cm^{-2}$. The capacitance plateau, between 2 and 20 $mV.s^{-1}$ is at 114 $mF.cm^{-2}$.

From the cyclic voltammetry at 1 $mV.s^{-1}$ (See Figure 8(c)), it is noteworthy to observe the current obtained with pseudocapacitance – a bump is visible around 0.5 V during oxidation and reduction which is impacting the total current. This bump indicates the presence of a redox mechanism involving the partial insertion of ions in the structure of MnO_2 at low scan rate.

In situ Raman spectroscopy.

The Raman signature of MnO_2 is mostly visible between 400 and 800 cm^{-1} with the presence of two main bands, ν_1 and ν_2 [14]. For birnessite MnO_2, ν_1 and ν_2 positions are around 620 - 650 cm^{-1} and around 580 - 590 cm^{-1} [15], respectively. They are assigned to the respective vibration modes of the symmetrical stretching and bending in the basal plane of Mn – O bonds [14,17–19]. The definition of these bands depends directly on the crystallinity of the MnO_2 [16]. As the MnO_2 characterized in this work is mostly amorphous, the resolution of these bands is limited.

Compared to aqueous electrolytes, the use of an ionic liquid as the electrolyte with birnessite-like MnO_2 utterly modifies the electrode material environment, with the absence of solvent affecting the cation intercalation mechanism. The use of *in situ* Raman spectroscopy can help to better understand these mechanisms, especially as the addition of alkaline salts (LiTFSI and NaTFSI) in the ionic liquid was seen to increase the pseudocapacitive role of MnO_2 [25].

Figure 9(a) shows the Raman spectra of the MnO_2 electrode in pure EMImTFSI at different charge states, offset with an intensity gap for better clarity. The black, cyan and purple spectra correspond respectively to the starting point where the electrode is reduced (polarization at -0,3 V vs Ag/Ag^+), in an oxidized state (+0,7 V vs Ag/Ag^+), and a final reduced state of the electrode (-0,3 V vs Ag/Ag^+). The spectra, obtained after the removal of EMImTFSI bands, show some defects around 300, 740 and 1250 cm^{-1}. We have applied a Bayesian Positive Source Separation (BPSS) decomposition procedure using our in-house developed method for solving curves. Due to the high noise and the low number of spectra, only a qualitative analysis is possible. Nonetheless it is possible to separate the signal into three distinct spectral sources, corresponding to IL without alkaline metal cations, a second source when the Li^+ cation is present, and a third source with Na^+ cation. Thus the Bayesian

decomposition of the signal sources demonstrates that the shifts discussed below are related to the presence of either lithium or sodium cations in the given ionic liquid.

As mentioned above, the two main bands related to Mn – O bonds are visible around 600 cm^{-1}. Figure 9(b) shows a zoom around these wavenumbers and, as expected, ν_1 and ν_2 can be seen at 620 - 650 cm^{-1} and 580 - 590 cm^{-1}, respectively.

The spectra are smoothed to help distinguish the evolution of ν_1 and ν_2 during the electrode cycling (See Figure 9(c)). Despite the noise, an evolution of the position of ν_1 and and ν_2 can be observed. Indeed, at the starting point with the electrode in a reduced state, ν_1 and ν_2 are centered at 633 and 587 cm^{-1}, respectively. After the oxidation of the electrode, the band positions move away from each other, shifting to 648 cm^{-1} for ν_1 and 578 cm^{-1} for ν_2. These band shifts are similar to those already observed in other works with MnO_2 electrodes in aqueous electrolytes [14,16,18,20]. This phenomenon may then be related to the evolution of the structure of MnO_2 with the insertion of ions into its structure (interlayer spacing) during reduction. Interlayer spaces are then closer when ions are intercalated (reduced state) and more spaced when ions are released back in the electrolyte (oxidized state).

When the reduced state of the electrode is reached again, the band positions have shifted to 630 and 588 cm^{-1}, respectively. These positions are close to those observed at the initial reduced state, which indicate a reversibility of the modifications of the MnO_2 structure occurring during cycling. This is in agreement with the phenomenon of pseudocapacitance attributed to MnO_2, which shows a breathing of the crystallographic structure during the cycling [28].

Figure 10 shows smoothed Raman spectra, between 200 and 900 cm^{-1}, of a MnO_2 electrode cycled in EMImTFSI + 0.5M LiTFSI and in EMImTFSI + 0.5M NaTFSI, respectively. The bands ν_1 and ν_2 can also be observed with these electrolytes, but with different shapes and intensities. These differences must be explained by the nature of the electrolyte, which leads to different interactions with the MnO_2 structure. Here, ν_1 and ν_2 are more distinct with sodium ions than with lithium ions.

With EMImTFSI + 0.5M LiTFSI as the electrolyte and at the starting point with a reduced electrode, ν_1 and ν_2 bands are respectively centered at 620 and 582 cm^{-1}. The band positions are shifting to 633 and 577 cm^{-1} when the electrode is oxidized, then shift back to 622 and 586 cm^{-1} after its reduction. The shift and its reversibility are similar to the ones observed above with pure EMImTFSI, but with different positions of ν_1 and ν_2. As it was highlighted in previous work, alkaline ions are participating in the pseudocapacitive reactions of MnO_2, together with the IL cations [25]. The presence of these lithium cations in the structure of MnO_2 when the electrode is oxidized must impact its structure, particularly the interlayer space, thus modifying the position of ν_1 and ν_2 bands.

The positions of ν_1 and ν_2 bands and their evolution in the system with NaTFSI are similar to those observed for the LiTFSI system, meaning that the cation addition leads to similar structural evolution of MnO_2 during cycling. At the starting point with a reduced electrode, ν_1 and ν_2 are centered at 618 and 587 cm^{-1}, respectively. The bands are respectively

shifting to 638 and 582 cm^{-1} after oxidation, then to 620 and 587 cm^{-1} after reduction of the electrode.

Figure 11 presents an overview of the positions and shifts of the ν_1 and ν_2 bands versus the charge of the electrode. This graph allows us to better picture the shifts of ν_1 and ν_2 and the differences between the three systems. In both systems, the band ν_2 has similar positions and is less impacted by the electrochemical cycling than ν_1. The band ν_1 gives more information. Indeed, its position, in systems with alkaline ions, is systematically a higher wavenumber than in the system with pure EMImTFSI. Regarding previous observations, a higher wavenumber of the band position is related to a smaller interlayer space [14,20]. This may be explained by stronger ionic interactions between MnO_2 and alkaline ion intercalated during reduction. This will be discussed below in the context of the DFT calculations.

As observed in previous work [6] and with the SPECS measurements previously depicted, alkaline ions are participating in the pseudocapacitive reactions, this implies that these cations must be intercalated partially in the interlayer space. However, the shift amplitude of ν_1 is similar for all systems, indicating that the modification of the MnO_2 structure (i.e. interlayer spacing) during the electrode cycling has a same amplitude for the three systems.

The $EMIm^+$ cation which is present in the three systems may be the origin of these similar behaviors. Due to their larger size and H-bonding ability, $EMIm^+$ cations appear to dominate the change in interlayer spacing upon cycling. This suggests that not only alkaline cations are intercalated in the MnO_2 interlayers upon reduction. Instead they are accompanied by $EMIm^+$ cations, which dictate the decrease in the interlayer distance upon reduction sweep. The reverse trend is observed upon the oxidation sweep where cations are leaving the interlayer space leading to its increase.

The smaller radii of lithium and sodium ions, compared to $EMIm^+$, suggest that these ions occupy vacant spaces that $EMIm^+$ ions cannot reach and that alkaline ions intercalation does not impact the interlayer space during the electrode cycling. The interlayer distance is thus fixed by intercalated $EMIm^+$ cations in all cases, and the alkaline cations enter in addition to the largest $EMIm^+$ cations' "pit prop" effect. Subsequently, with additional alkaline cations, the ionic density is higher for a same volume, which translate to a larger number of ions participating to the pseudocapacitive charge storage, leading to an increase in the overall capacitance as also observed from the SPECS measurements.

The presence of redox bumps observed in the cyclic voltammograms obtained from SPECS measurements in Figure 7(c) and Figure 8(c) is then in good agreement with these assumptions. Both SPECS and *in situ* Raman analysis indicate that cation intercalation occurs upon reduction and that this process is reversible. Moreover, the structural change related to this intercalation and more specifically the width of the interlayer spacing is ruled by the presence of intercalated $EMIm^+$ cations, while the value of the capacity related to this phenomenon is ruled by the number of co-intercalated Li^+ or Na^+ cations.

DFT calculations.

The cationic intercalation behavior is examined further via DFT calculations. The three-atom unit cell for monolayer MnO_2 system relaxes to a 2D-hexagonal layer of edge-joined octahedra with in-plane lattice parameter 2.924 Å, adopting a 3μB/MnO_2 unit spin state in agreement with literature (see Figure S4) [29]. The multi-layered MnO_2 structure (starting from symmetry broken triclinic to avoid symmetry trapping) with no interlayer species spontaneously relaxes to AA-stacked hexagonal layers. The three-atom unit cell requires high k-point density (in this case at least 6x6x6); doubling the k-point grid changed the unit cell parameters by less than 0.001 Å. The spacing between Mn layers is then 4.251 Å (i.e. the distance between planes defined by the average Mn atom centre positions in each

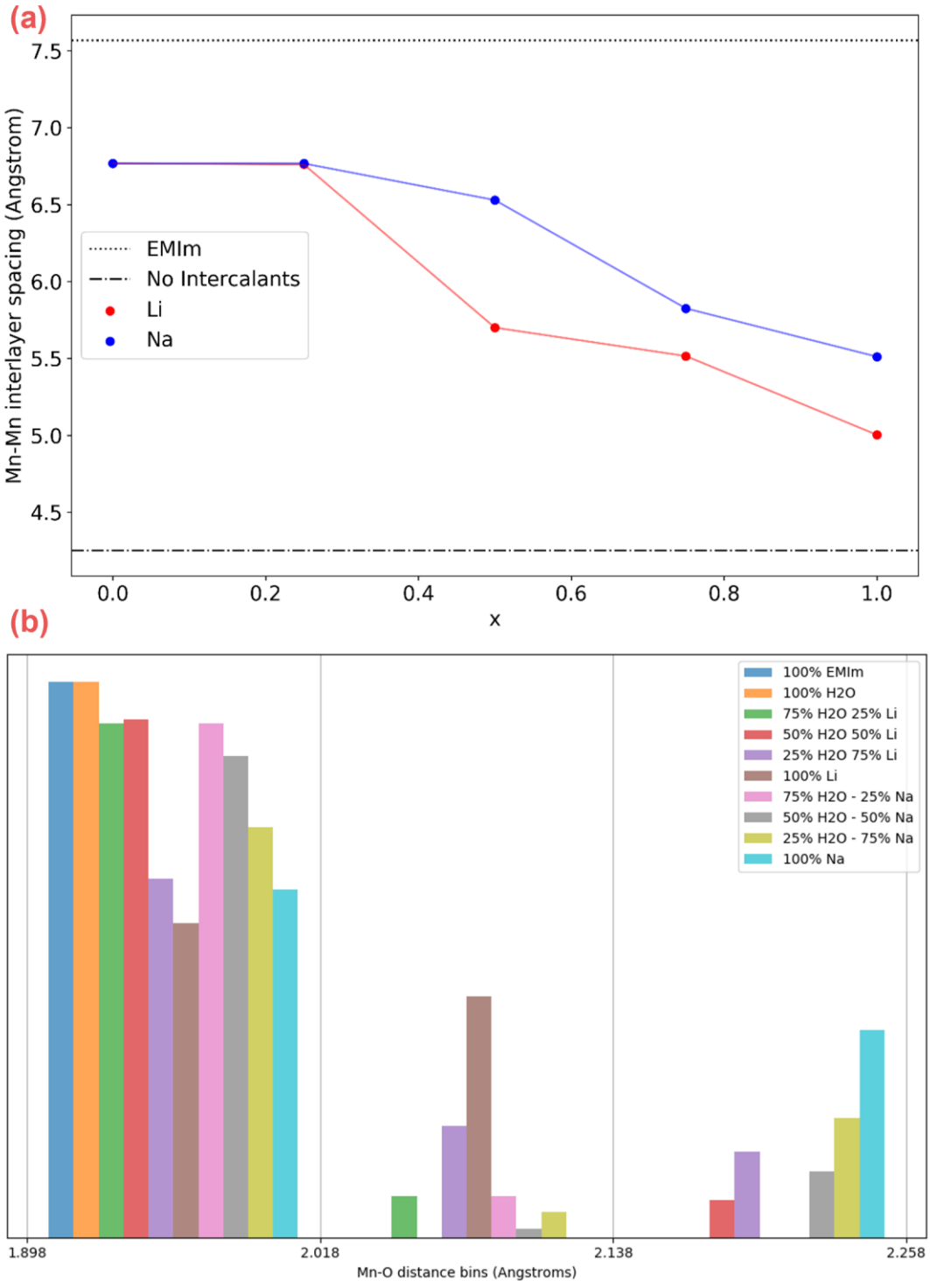

layer,

Figure 12(a)). System spin is varied, the system adopts a stable spin state of $3\mu_B$/Mn atom, in agreement with literature. Experimentally, birnessite is a hydrous phase with a water layer between the MnO_2 sheets, with exact composition varying depending on the salt concentration of the water. When we add water giving $MnO_2.H_2O$

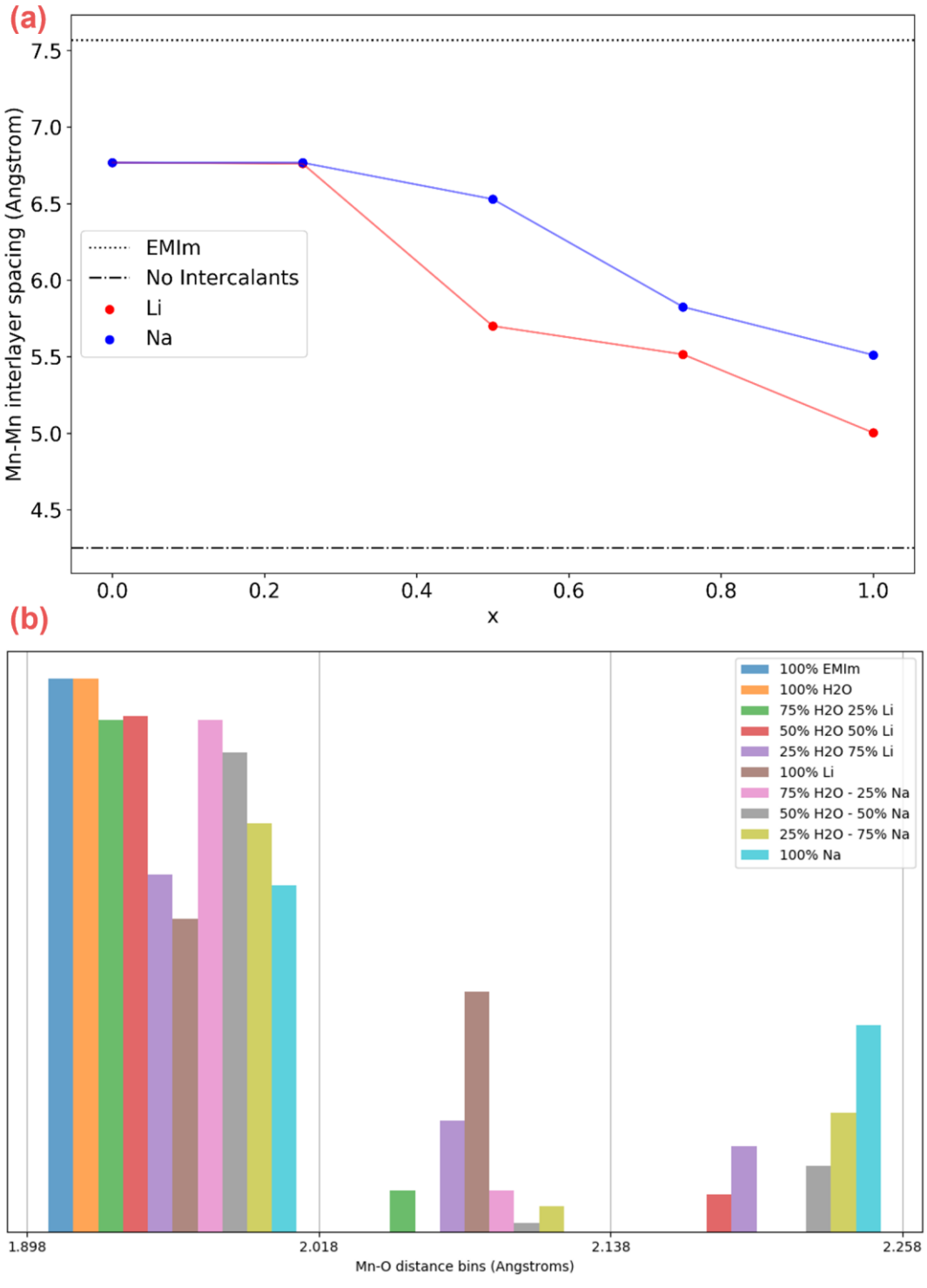

(

Figure 12(b)) the interlayer spacing increases to 7.040 Å, in good agreement with experimental literature value of 7.19 Å (noting that the experimental material also contains vacancies and interlayer Mn cations) [30].

Using a 2x2 supercell allows exploration of sequential Li and Na intercalation, i.e. $MnO_2.M_x(H_2O)_{1-x}$ (M=Li, Na, x=0, 0.25, 0.5, 0.75, 1). System spin is varied, the most stable structure consisting of $(4-x)Mn^{4+}$ atoms with spin $3\mu_B$ and xMn^{3+} atoms with spin $4\mu_B$, due to

charge transfer from the intercalated metal.

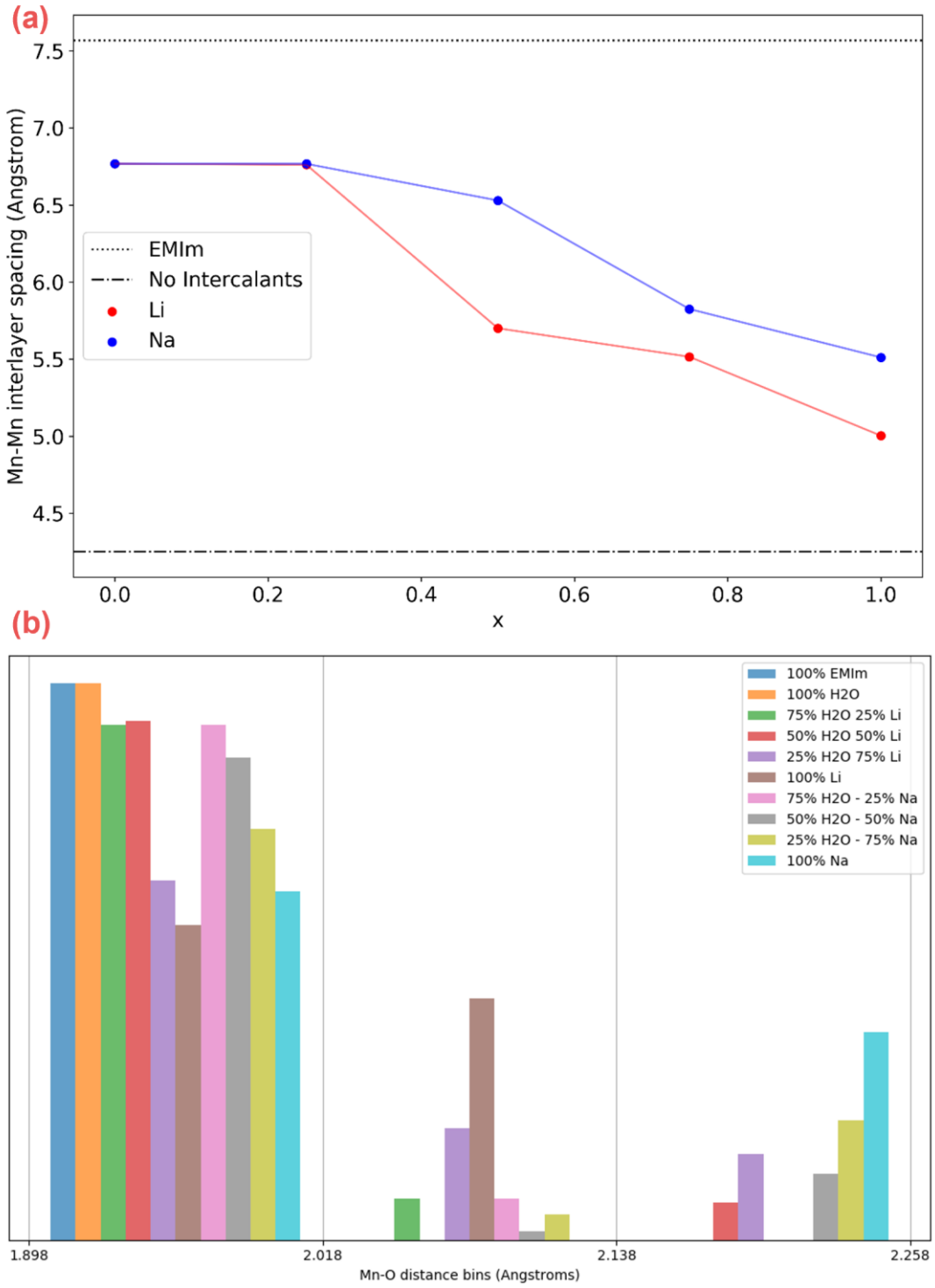

Figure 12(a) and Table 1 show the variation in interlayer spacing with increasing Li^+/Na^+ concentration. Initial metal intercalation does not strongly change interlayer spacing since the remaining H_2O dominates, but as the H_2O is increasingly substituted the interlayer spacing drops, with the change most notable for the smaller Li ion. At 100% metal substitution of the H_2O, interlayer spacing drops by 1.764 Å and 1.256 Å for Li^+ and Na^+ respectively.

In contrast, insertion of $EMIm^+$ causes an increase in the interlayer spacing of 0.800 Å, the $EMIm^+$ preferentially adopting a flat configuration with the methyl group lying in the molecular plane (rotating the methyl group perpendicular to the molecular is 0.84 eV less stable and thermodynamically unlikely to occur). As such intercalated $EMIm^+$ should dominate interlayer spacing, holding the layers a fixed distance apart independent of $Li^+/Na^+/H_2O$ (de)intercalation processes. However, significant substitution of $EMIm^+$ by Li^+/Na^+ will lead to a gradual decrease in interlayer spacing, similar to that seen with the water.

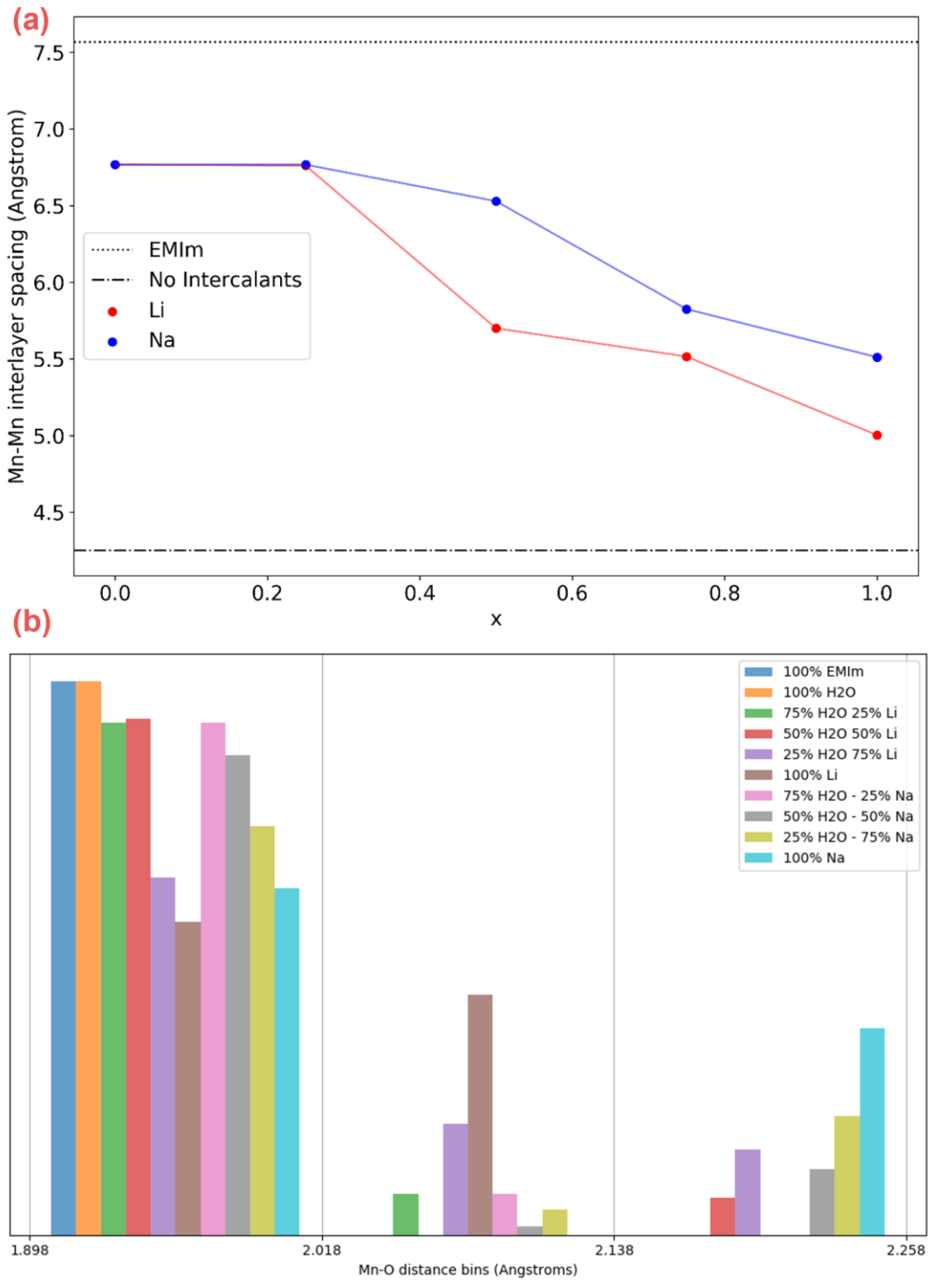

Figure 12(b) shows the change in Mn-O bond lengths with intercalation, as the associated Jahn-Teller distortion and Mn charge results in symmetry breaking. The bond lengths follow the overall trend in the experimental Raman signature, with a shift to increased Mn-O lengths with increasing metal intercalation. The fluctuations in the histogram of bond lengths reflect symmetry breaking due to variations in the hydrogen bonding networks that form between the remaining water molecules. For $EMIm^+$ a larger 3x3 supercell is required to incorporate the molecule and hence has lower concentration of $EMIm(MnO_2)_9$, which helps explain why the Mn-O bond lengths are largely restored to their hydrated values when $EMIm^+$ is intercalated.

The $LiMnO_2$ result demonstrates that interlayer stacking translation plays only a minor role, since the interlayer spacing for ABC-stacked triple layers from GGA(PBE)+U calculations is close to ours at 4.829 Å [31,32]. The difference in interlayer spacing between $LiMnO_2$ and non-hydrated MnO_2 is 0.752 Å, close to the Li^+ effective ionic radius (0.76 Å). $NaMnO_2$, also results in distortion of the triclinic cell, with Mn-Mn distances varying between 2.91 and 3.24 Å, as previously observed in the literature [33]. The difference in interlayer spacing between MnO_2 and $NaMnO_2$ of 1.260 Å is this time slightly higher than the Na^+ effective ionic radius (1.02 Å).

In summary, substitutional insertion of Li^+ and Na^+ into hydrated $MnO_2.H_2O$ leads to a decrease in interlayer spacing of up to 1.764 Å and 1.256 Å for Li^+ and Na^+ respectively. Note however that spacing change is not linear with metal concentration; at 50% Na^+ substitution (already a high metal concentration) the decrease is only 0.238 Å. This is similar to 0.35 Å variations seen in interlayer spacing by in-situ X-ray diffraction (XRD) in Na-cycled MnO_2 [20]. In contrast, water substitution by $EMIm^+$ increases interlayer spacing by 0.800 Å, the $EMIm^+$ lying with its methyl group in the molecular plane. Thus, we expected that $EMIm^+$ intercalation will dominate interlayer spacing behaviour, holding the layers apart and facilitating rapid Li^+/Na^+ (de)intercalation. Only in zones where $EMIm^+$ is substituted by Li^+/Na^+ will the interlayer spacing drop. In these cases, a higher ion density can be achieved, resulting in local increases in Mn-O bond lengths and corresponding shifts in Mn-O Raman frequencies.

Conclusions

The two spectroscopy methods presented in this work allow an in-depth understanding of the charge storage behavior of MnO_2 thin film electrodes in ionic liquid-based supercapacitors. Firstly, the Step Potential ElectroChemical Spectroscopy (SPECS) was used to characterize MnO_2 electrodes in ionic liquids. The current delivered by the electrode, in pure EMImTFSI, EMImTFSI + 0.5M LiTFSI and EMImTFSI + 0.5M NaTFSI, was separated between double layer capacitance, pseudocapacitance, diffusion and side reactions with this technique. The reconstruction of capacitance contributions for each system highlighted the role of pseudocapacitance itself and also of alkaline ion addition, which are increasing the pseudocapacitive charge storage component with respect to overall capacitance. The voltammograms obtained in ternary ionic liquids at low scan rates present redox peaks indicating a partial ion intercalation in the MnO_2 structure.

This latter observation motivated the use of *in situ* Raman spectroscopy to obtain a better understanding of the mechanisms occurring during the cycling of MnO_2-based electrode. For the first time, this technique was performed on MnO_2 electrodes in ionic liquid electrolytes. Monitoring of one full cycle of oxidation and reduction of the electrode shows the evolution of the structure of MnO_2, with a smaller interlayer space at the reduced state when ions are intercalated and a larger interlayer space when ions are deintercalated at the oxidized state. The comparison of the position of Raman bands related to the Mn – O bounds as well as DFT results show a difference between systems with doped ionic liquids and pure ionic liquid: the presence of alkaline ions decreases the interlayer space due to stronger ionic interactions. However, independently of the presence or nature of alkaline cations, the "breathing" of the interlayer space during oxidation and reduction is of the same amplitude. According to this observation and DFT results on the $EMIm^+$ ion intercalation, it seems the ionic liquid cation is defining the interlayer space in birnessite MnO_2. Additional alkaline cations may then occupy specific vacancies inaccessible by the ionic liquid cations, increasing the ionic density without further volumetric changes. This may explain the redox peak on voltammograms and the larger pseudocapacitive part observed with SPECS with the presence of alkaline cations.

Acknowledgments

This work was supported by the ANR French agency through the DENSSCAPIO project (ANR-17-CE05-0015). The authors declare no conflict of interest. The authors also want to thank the ANR STORE-EX (ANR-10LABX-76-01) and the French network on electrochemical energy storage (RS2E) for the financial support. CNRS and MAE are also greatly acknowledged for supporting French-Australian PseudoSPECS PROJECT (IEA 2019).

References

1. Singh SK, Savoy AW. Ionic liquids synthesis and applications: An overview. *Journal of Molecular Liquids*. 2020;297:112038. doi:10.1016/j.molliq.2019.112038

2. Wang X, Salari M, Jiang D en, et al. Electrode material–ionic liquid coupling for electrochemical energy storage. *Nat Rev Mater*. 2020;5(11):787-808. doi:10.1038/s41578-020-0218-9

3. Stettner T, Balducci A. Protic ionic liquids in energy storage devices: past, present and future perspective. *Energy Storage Mater*. 2021;40:402-414. doi:10.1016/j.ensm.2021.04.036

4. Brousse T, Bélanger D, Long JW. To Be or Not To Be Pseudocapacitive? *J Electrochem Soc*. 2015;162(5):A5185-A5189. doi:10.1149/2.0201505jes

5. Lee HY, Goodenough JB. Supercapacitor Behavior with KCl Electrolyte. *Journal of Solid State Chemistry*. 1999;144(1):220-223. doi:10.1006/jssc.1998.8128

6. Toupin M, Brousse T, Bélanger D. Influence of Microstucture on the Charge Storage Properties of Chemically Synthesized Manganese Dioxide. *Chem Mater*. 2002;14(9):3946-3952. doi:10.1021/cm020408q

7. Toupin M, Brousse T, Bélanger D. Charge Storage Mechanism of MnO_2 Electrode Used in Aqueous Electrochemical Capacitor. *Chem Mater*. 2004;16(16):3184-3190. doi:10.1021/cm049649j

8. Zhang J, Li W, Wang J, et al. Engineering p-Band Center of Oxygen Boosting H^+ Intercalation in δ-MnO_2 for Aqueous Zinc Ion Batteries. *Angewandte Chemie International Edition*, 2023, vol. 62, no 8, p. e202215654. doi:10.1002/anie.202215654

9. Castro Ruiz CA, Bélanger D, Rochefort D. Electrochemical and Spectroelectrochemical Evidence of Redox Transitions Involving Protons in Thin MnO_2 Electrodes in Protic Ionic Liquids. *J Phys Chem C*. 2013;117(40):20397-20405. doi:10.1021/jp405047g

10. Eustache E, Douard C, Retoux R, Lethien C, Brousse T. MnO_2 Thin Films on 3D Scaffold: Microsupercapacitor Electrodes Competing with “Bulk” Carbon Electrodes. *Advanced Energy Materials*. 2015;5(18):1500680. doi:10.1002/aenm.201500680

11. Dupont MF, Donne SW. A Step Potential Electrochemical Spectroscopy Analysis of Electrochemical Capacitor Electrode Performance. *Electrochimica Acta*. 2015;167:268-277. doi:10.1016/j.electacta.2015.03.137

12. Dupont MF, Donne SW. Separating Faradaic and Non-Faradaic Charge Storage Contributions in Activated Carbon Electrochemical Capacitors Using Electrochemical Methods: I. Step Potential Electrochemical Spectroscopy. *J Electrochem Soc*.

2015;162(7):A1246-A1254. doi:10.1149/2.0611507jes

13. Dupont MF, Donne SW. Separating the Faradaic and Non-Faradaic Contributions to the Total Capacitance for Different Manganese Dioxide Phases. *J Electrochem Soc*. 2015;162(5):A5096-A5105. doi:10.1149/2.0161505jes

14. Chen D, Ding D, Li X, et al. Probing the Charge Storage Mechanism of a Pseudocapacitive MnO_2 Electrode Using *in Operando* Raman Spectroscopy. *Chem Mater*. 2015;27(19):6608-6619. doi:10.1021/acs.chemmater.5b03118

15. Bernardini S, Bellatreccia F, Casanova Municchia A, Della Ventura G, Sodo A. Raman spectra of natural manganese oxides. *J Raman Spectrosc*. 2019;50(6):873-888. doi:10.1002/jrs.5583

16. Yang L, Cheng S, Wang J, et al. Investigation into the origin of high stability of δ-MnO_2 pseudo-capacitive electrode using operando Raman spectroscopy. *Nano Energy*. 2016;30:293-302. doi:10.1016/j.nanoen.2016.10.018

17. Hsu YK, Chen YC, Lin YG, Chen LC, Chen KH. Reversible phase transformation of MnO_2 nanosheets in an electrochemical capacitor investigated by in situ Raman spectroscopy. *Chem Commun*. 2011;47(4):1252-1254. doi:10.1039/C0CC03902K

18. Julien C, Massot M, Baddour-Hadjean R, Franger S, Bach S, Pereira-Ramos JP. Raman spectra of birnessite manganese dioxides. *Solid State Ionics*. 2003;159(3-4):345-356. doi:10.1016/S0167-2738(03)00035-3

19. Julien C. Local Environment in 4-Volt Cathode Materials for Li-Ion Batteries. In: Julien C, Stoynov Z, eds. *Materials for Lithium-Ion Batteries*. Springer Netherlands; 2000:309-326. doi:10.1007/978-94-011-4333-2_13

20. Scheitenberger P, Brimaud S, Lindén M. XRD/Raman spectroscopy studies of the mechanism of (de)intercalation of Na^+ from/into highly crystalline birnessite. *Mater Adv*. 2021;2(12):3940-3953. doi:10.1039/D1MA00161B

21. Julien C, Massot M, Rangan S, Lemal M, Guyomard D. Study of structural defects in γ-MnO_2 by Raman spectroscopy. *J Raman Spectrosc*. 2002;33(4):223-228. doi:10.1002/jrs.838

22. Lindberg S, Jeschke S, Jankowski P, et al. Charge storage mechanism of α-MnO2 in protic and aprotic ionic liquid electrolytes. *J Power Sources*. 2020;460:228111. doi:10.1016/j.jpowsour.2020.228111

23. Eustache E, Douard C, Demortière A, et al. High Areal Energy 3D-Interdigitated Micro-Supercapacitors in Aqueous and Ionic Liquid Electrolytes. *Advanced Materials*

Technologies. 2017;2(10):1700126. doi:10.1002/admt.201700126

24. Asbani B, Douard C, Brousse T, Le Bideau J. High temperature solid-state supercapacitor designed with ionogel electrolyte. *Energy Storage Materials*. 2019;21:439-445. doi:10.1016/j.ensm.2019.06.004

25. Guillemin T, Douard C, Robert K, et al. Solid-state 3D micro-supercapacitors based on ionogel electrolyte: Influence of adding lithium and sodium salts to the ionic liquid. *Energy Storage Materials*. 2022;50:606-617. doi:10.1016/j.ensm.2022.05.041

26. Bounor B, Asbani B, Douard C, Favier F, Brousse T, Lethien C. On chip MnO_2-based 3D micro-supercapacitors with ultra-high areal energy density. *Energy Storage Materials*. 2021;38:520-527. doi:10.1016/j.ensm.2021.03.034

27. Forghani M, Donne SW. Modification of the Step Potential Electrochemical Spectroscopy Analysis Protocol to Improve Outcomes. *Journal of The Electrochemical Society*. 2019;166:A2727-A2737. doi:10.1149/2.0091913jes/meta

28. Athouël L, Moser F, Dugas R, Crosnier O, Bélanger D, Brousse T. Variation of the MnO_2 Birnessite Structure upon Charge/Discharge in an Electrochemical Supercapacitor Electrode in Aqueous Na_2SO_4 Electrolyte. *J Phys Chem C*. 2008;112(18):7270-7277. doi:10.1021/jp0773029

29. Jain A, Ong SP, Hautier G, et al. Commentary: The Materials Project: A materials genome approach to accelerating materials innovation. *APL Materials*. 2013;1(1):011002. doi:10.1063/1.4812323

30. Drits VA, Silvester E, Gorshkov AI, Manceau A. Structure of synthetic monoclinic Na-rich birnessite and hexagonal birnessite; I, Results from X-ray diffraction and selected-area electron diffraction. *American Mineralogist*. 1997;82(9-10):946-961. doi:10.2138/am-1997-9-1012

31. Tsebesebe NT, Kgatwane KM, Ledwaba RS, Ngoepe PE. Investigating the Structural and Electronic Properties of $LiMO_2$ (M: Mn, Ni, Co) as Potential Cathode Materials: A DFT Study. *J Phys: Conf Ser*. 2022;2298(1):012010. doi:10.1088/1742-6596/2298/1/012010

32. Armstrong AR, Dupre N, Paterson AJ, Grey CP, Bruce PG. Combined Neutron Diffraction, NMR, and Electrochemical Investigation of the Layered-to-Spinel Transformation in $LiMnO_2$. *Chem Mater*. 2004;16(16):3106-3118. doi:10.1021/cm034964b

33. Vitoux L, Guignard M, Penin N, Carlier D, Darriet J, Delmas C. $NaMoO_2$: a Layered Oxide with Molybdenum Clusters. *Inorg Chem*. 2020;59(6):4015-4023. doi:10.1021/acs.inorgchem.9b03688

Tables

Table 1 : DFT calculated interlayer spacing (Mn-Mn) as a function of intercalated metal species in $MnO_2.M_x(H_2O)_{1-x}$, M=Li, Na. Also included is MnO_2 with no intercalated species for comparison, and with intercalated $EMIm^+$ (see text).

		Interlayer Spacing (Å)	
% Metal	**% H2O**	**Na^+**	**Li^+**
0	**100**	**6.767**	
25	**75**	**6.767**	**6.761**
50	**50**	**6.529**	**5.700**
75	**25**	**5.825**	**5.515**
100	**0**	**5.511**	**5.003**
0	**0**	**4.251**	
$EMIm^+$	**0**	**7.567**	

Figures

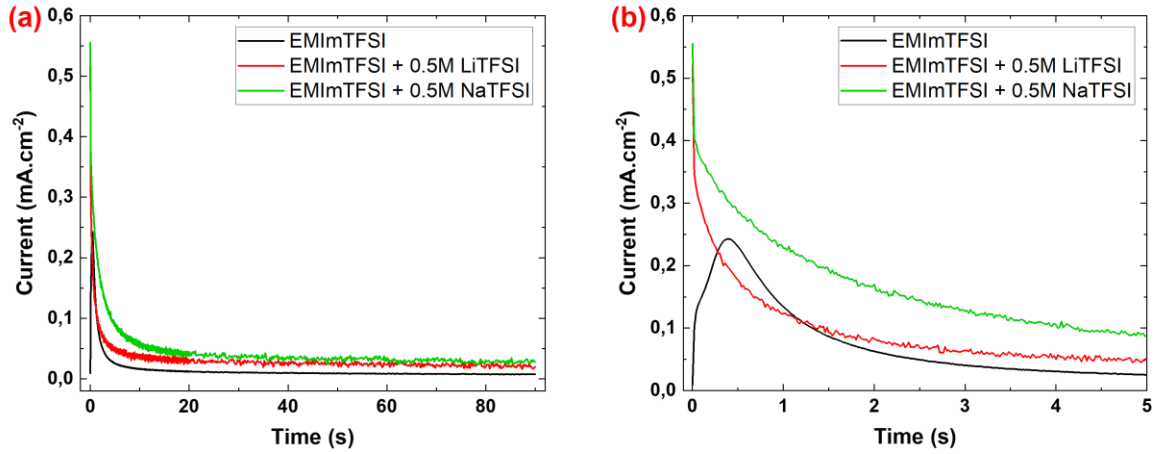

Figure 1 : (a) Current vs time evolution, measured during one potentiostatic step (90 s duration). (b) Zoom on the current evolution at the first seconds of the step.

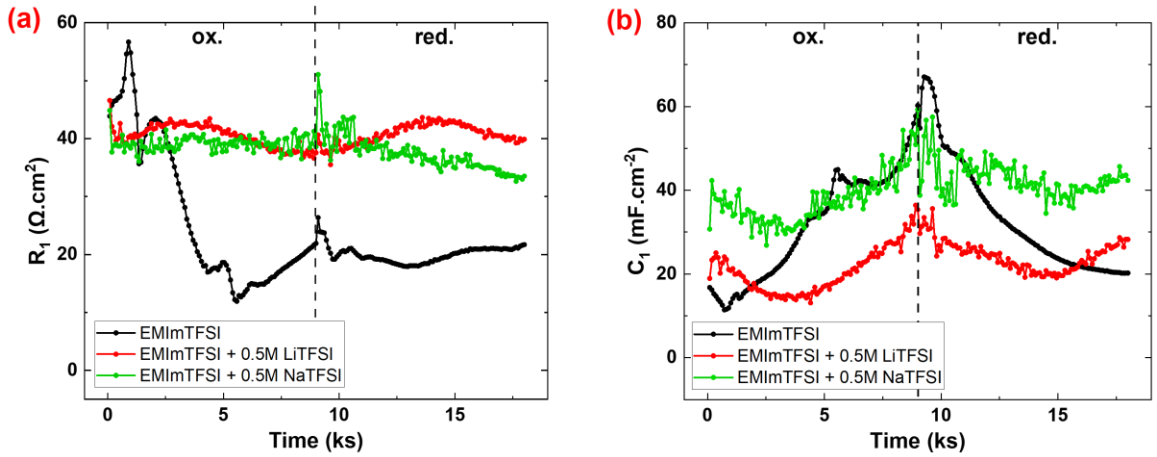

Figure 2 : Evolution of (a) resistances R_1 and (b) capacitance C_1, attributed to electrode surface mechanisms, during SPECS measurement. Oxidation and reduction are separated by the vertical dotted line.

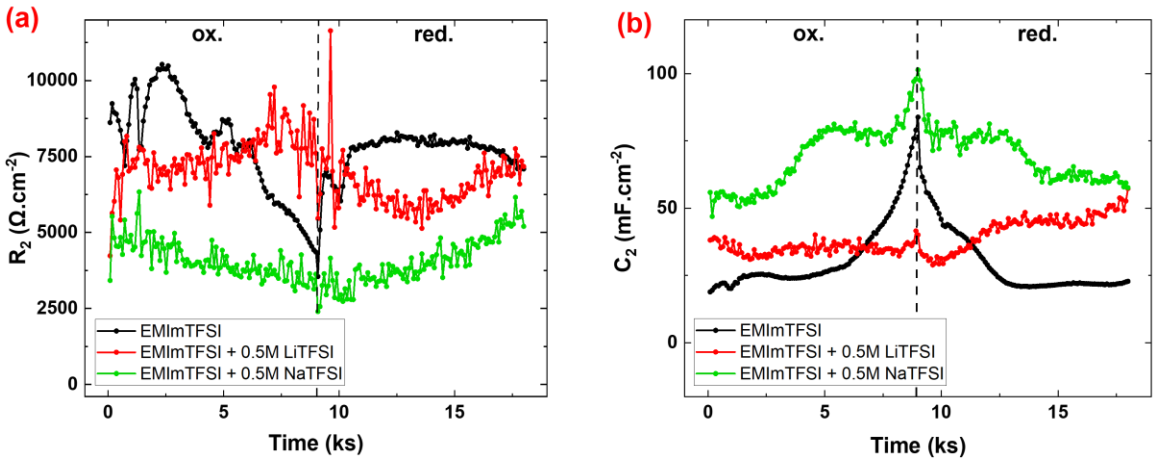

Figure 3 : Evolution of (a) resistances R_2 and (b) capacitance C_2, attributed to electrode surface mechanisms, during SPECS measurement. Oxidation and reduction are separated by the vertical dotted line.

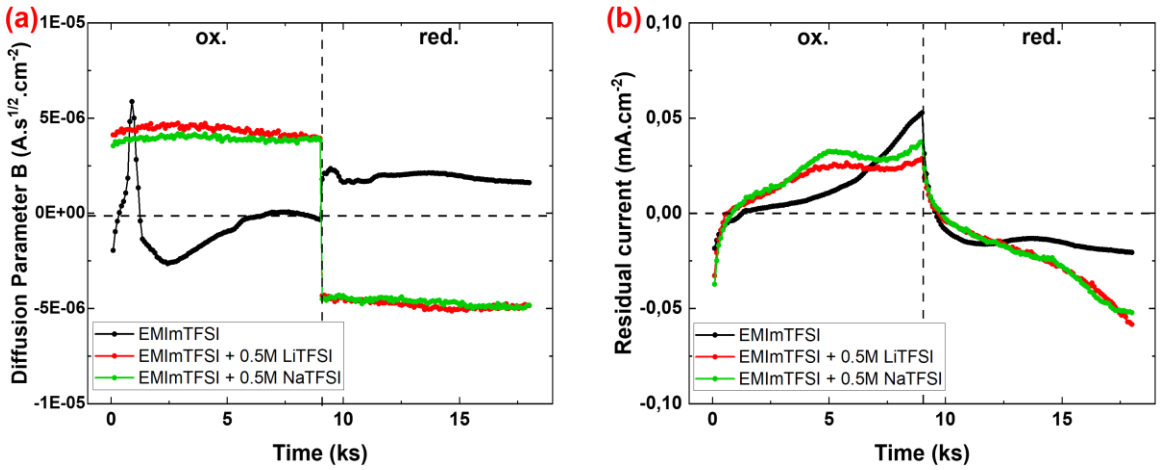

Figure 4 : Evolution of (a) the diffusion parameter and (b) the residual current. Oxidation and reduction are separated by the vertical dotted line.

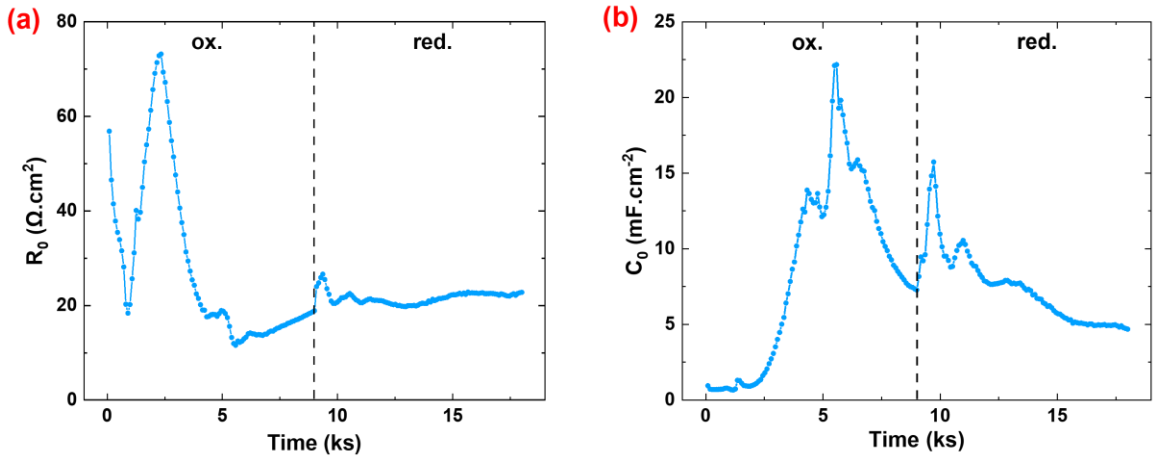

Figure 5 : Evolution of (a) resistance R_0 and (b) capacitance C_0 during SPECS measurement. These parameters are only used for the system with pure EMImTFSI.

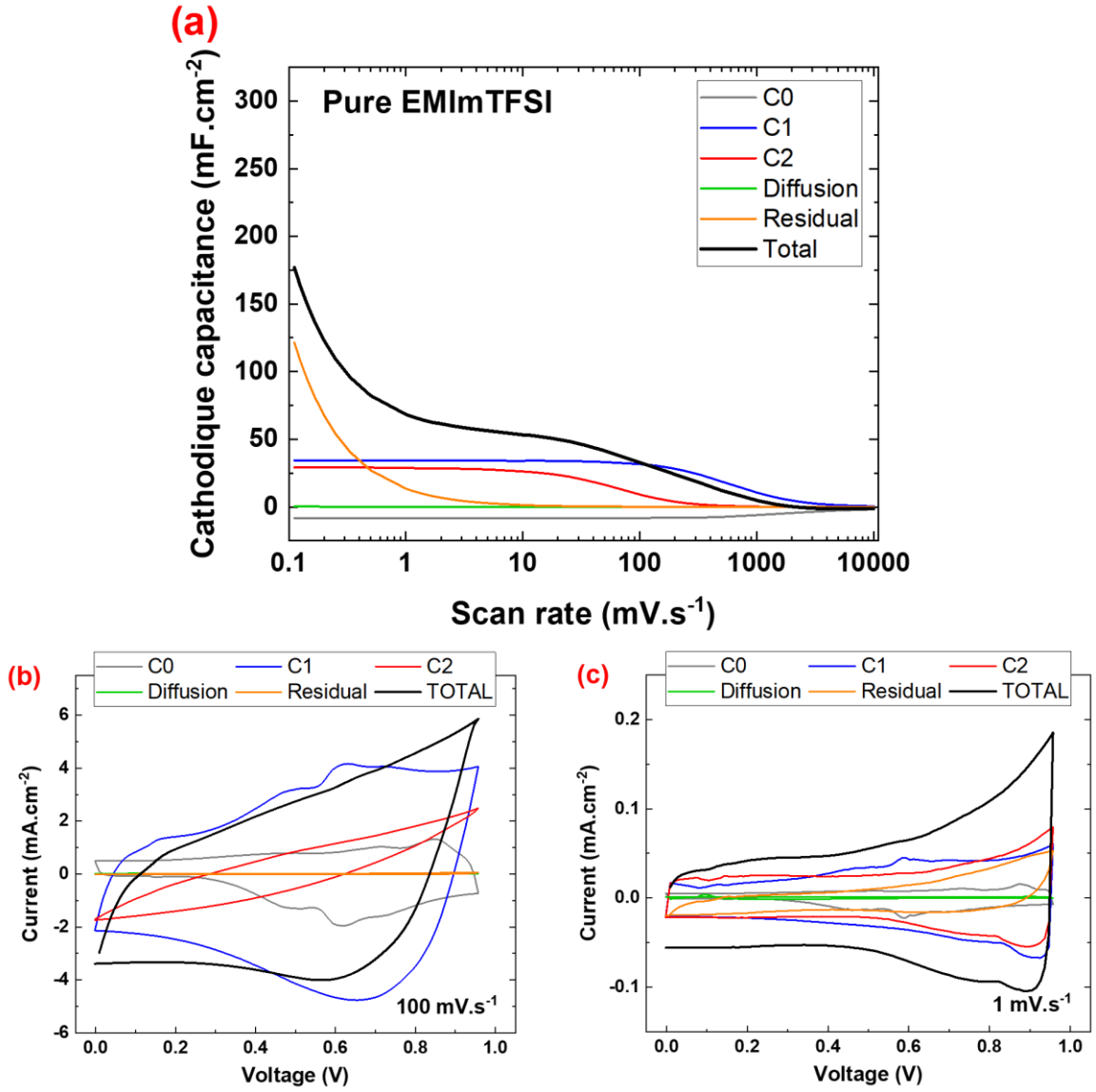

Figure 6 : (a) Evolution of capacitance versus scan rate for each contribution to the total current in pure EMImTFSI. (b) Cyclic voltammetry reconstruction for each contribution at 100 $mV.s^{-1}$ and (c) at 1 $mV.s^{-1}$.

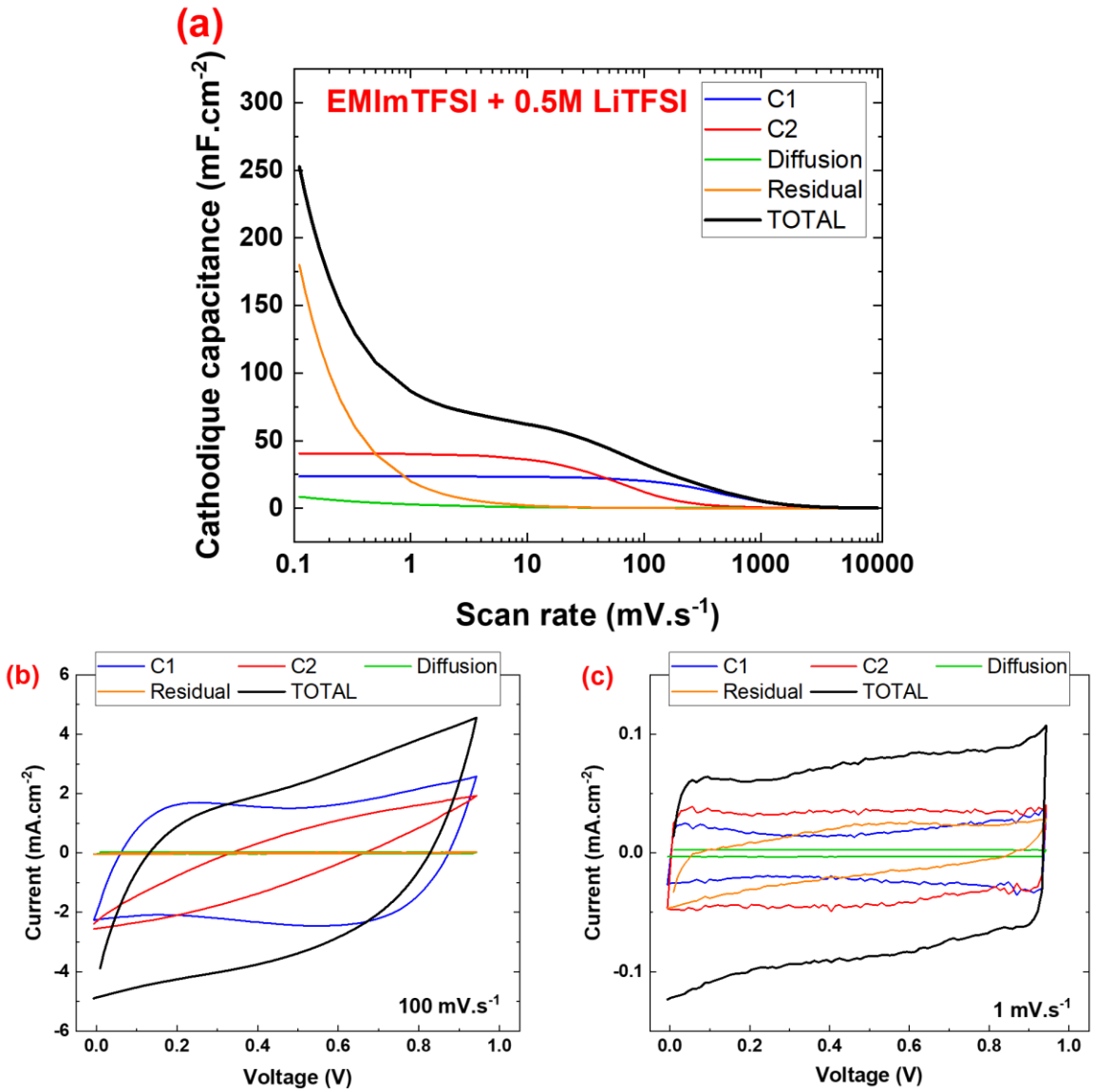

Figure 7 : (a) Evolution of capacitance versus scan rate for each contribution to the total current in EMImTFSI + 0.5M LiTFSI. (b) Cyclic voltammetry reconstruction for each contribution at 100 $mV.s^{-1}$ and (c) at 1 $mV.s^{-1}$.

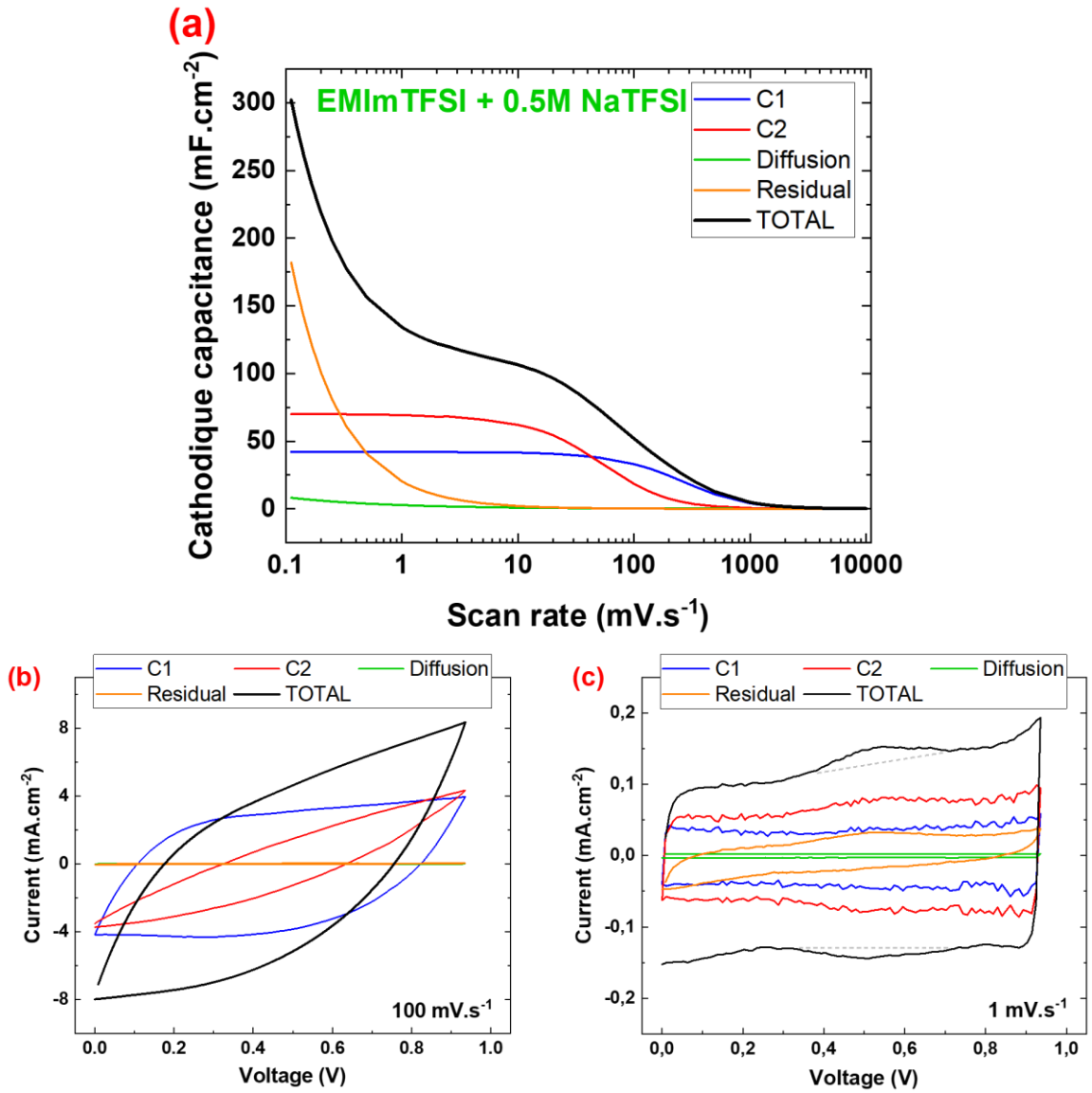

Figure 8 : (a) Evolution of capacitance versus scan rate for each contribution to the total current in pure EMImTFSI + 0.5M NaTFSI. (b) Cyclic voltammetry reconstruction for each contribution at 100 $mV.s^{-1}$ and (c) at 1 $mV.s^{-1}$. The dashed gray line are guidelines for the eyes to emphasize the presence of broad redox peaks on the black plot.

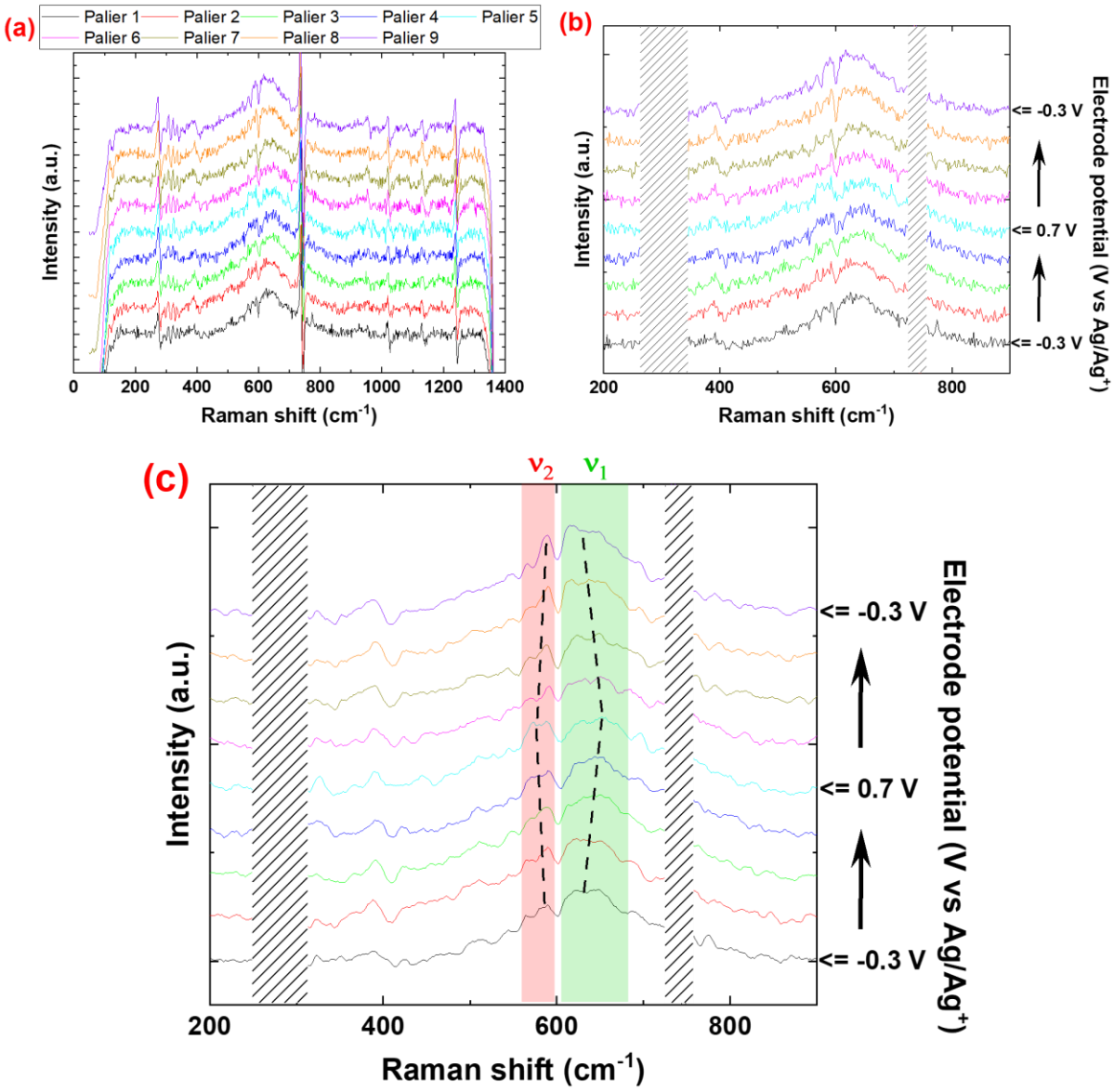

Figure 9 : Raman spectra of the MnO_2 electrode in pure EMImTFSI, (a) between 50 and 1400 cm^{-1} after removal of EMImTFSI bands, (b) between 200 and 900 cm^{-1} and (c) after smoothing noise. Hatched parts cover defects after the removal of EMImTFSI spectrum, for a better legibility.

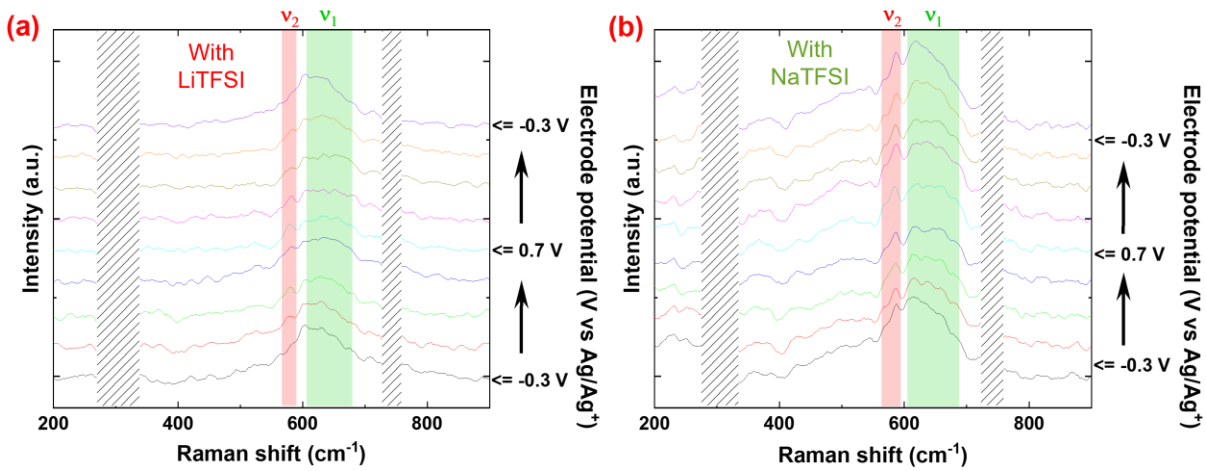

Figure 10 : Raman spectra, between 200 and 900 cm^{-1} and after noise smoothing, of a MnO_2 electrode in (a) EMImTFSI + 0.5M LiTFSI an (b) EMImTFSI + 0.5M NaTFSI.

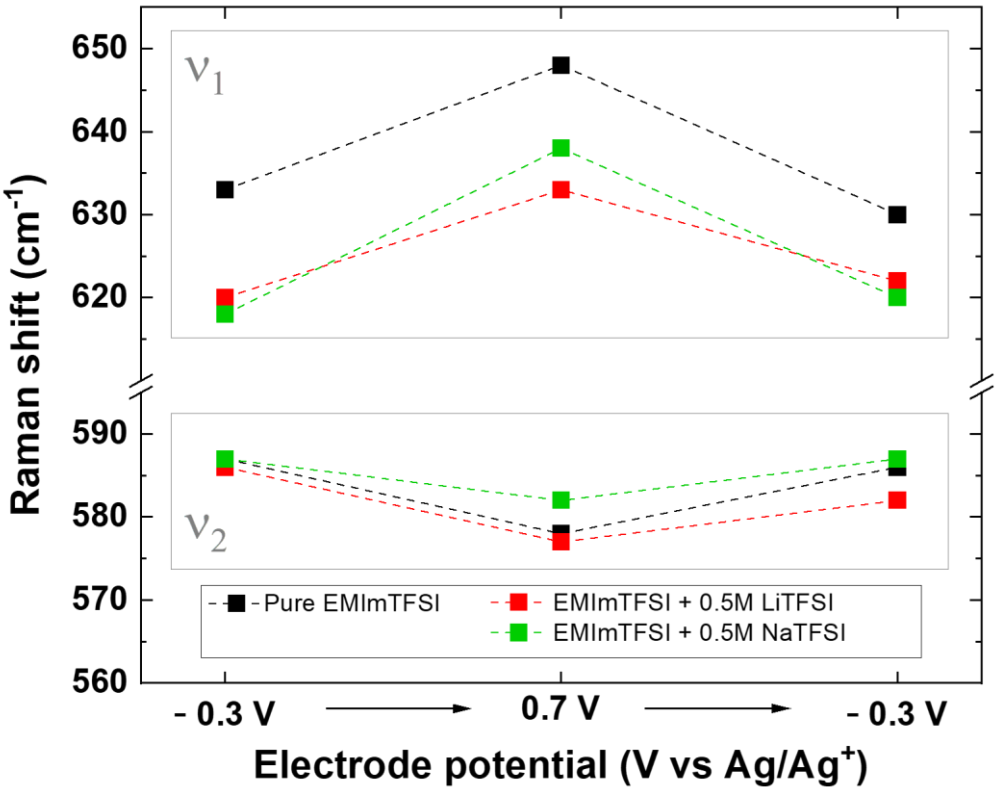

Figure 11 : Evolution of the positions of ν_1 and ν_2 bands versus the charge state of the electrode and the electrolyte used.

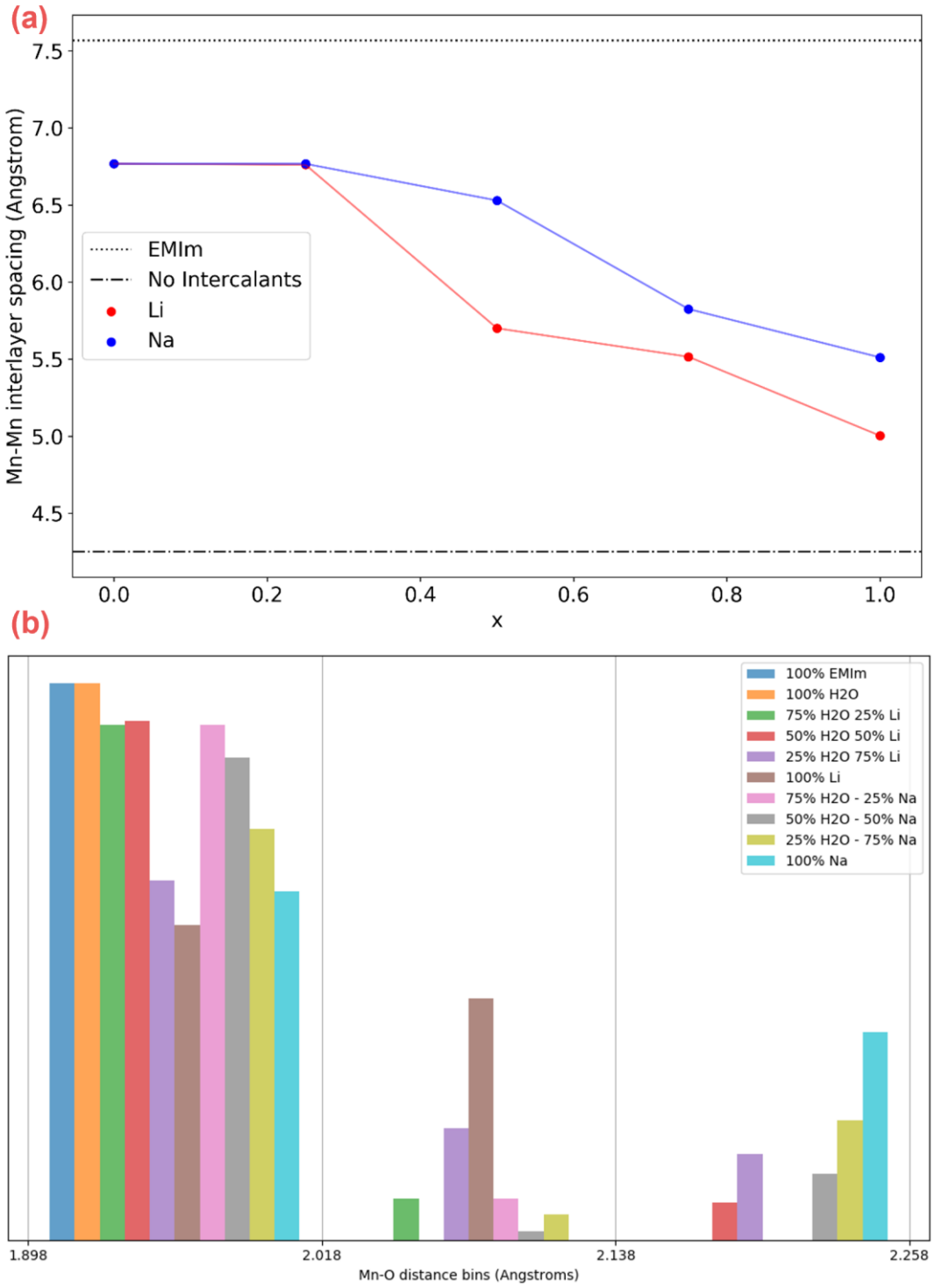

Figure 12 : (a) Mn-Mn interlayer spacing (Å), x-axis indicates $MnO_2.M_x(H_2O)_{(1-x)}$, M=Li, Na. MnO_2.EMim and MnO_2 are marked as dotted lines. (b) Histogram of DFT calculated Mn-O bond lengths (Å) for MnO_2 with various intercalated species.

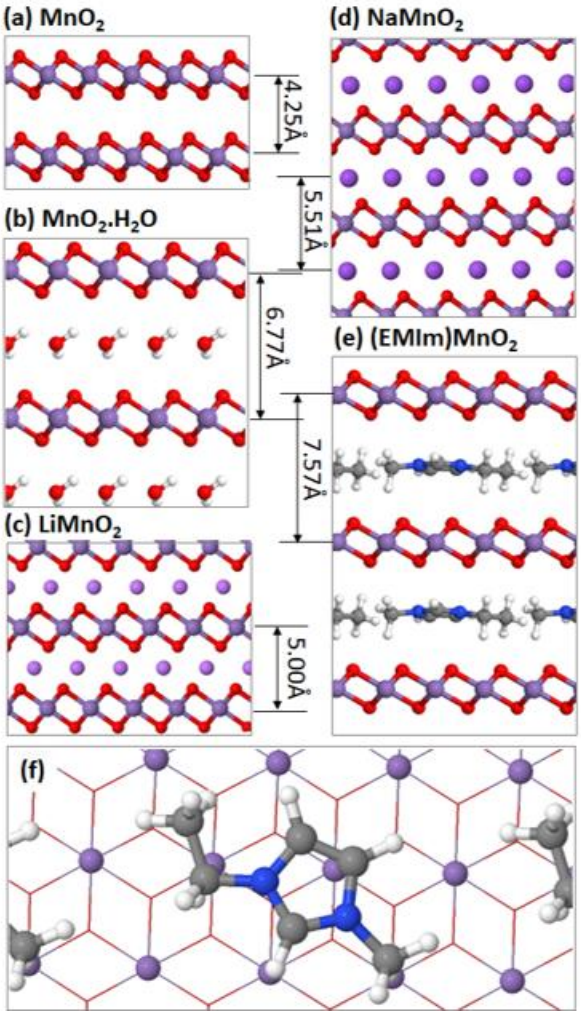

Figure 13: DFT optimized layered MnO_2 structures showing interlayer spacing (a) pure MnO_2, (b) $MnO_2.H_2O$, (c) $LiMnO_2$, (d) $NaMnO_2$ and (d,e) $EMIm^+$. Mn-Mn interlayer spaces in Å. In (e), oxygen atoms are hidden and Mn-O bonds drawn wireframe for clarity.